Advanced Fiber Materials (2025) 7:1590–1604
https://doi.org/10.1007/s42765-025-00572-3

RESEARCH ARTICLE

Textile-Based Mechanoreceptor Array with Tunable Pressure Thresholds for Mutli-dimensional Detection in Healthcare Monitoring

Kitming Ma[1,2] · Linlin Ma[1,2] · Chengyu Li[1,2] · Renbo Zhu[1,2] · Jing Yang[1,2] · Su Liu[1,2] · Xiaoming Tao[1,2]

Received: 5 February 2025 / Accepted: 22 May 2025 / Published online: 16 June 2025

Abstract

Mimicking human skin mechanoreceptors grouped by various thresholds creates an efficient system to detect interfacial stress between skin and environment, enabling precise human perception. Specifically, the detected signals are transmitted in the form of spikes in the neuronal network via synapses. However, current efforts replicating this mechanism for health-monitoring struggle with limitations in flexibility, durability, and performance, particularly in terms of low sensitivity and narrow detection range. This study develops novel soft mechanoreceptors with tunable pressure thresholds from 1.94 kPa to 15 MPa. The 0.455-mm-thin mechanoreceptor achieves an impressive on–off ratio of over eight orders of magnitude, up to 40,000 repeated compression cycles and after 20 wash cycles. In addition, the helical array reduces the complexity and port count, requiring only two output channels, and a differential simplification algorithm enables two-dimensional spatial mapping of pressure. This array shows stable performance across temperatures ranging from −40 to 50 °C and underwater at depths of 1 m. This technology shows significant potential for wearable healthcare applications, including sensor stimulation for children and the elderly, and fall detection for Parkinson's patients, thereby enhancing the functionality and reliability of wearable monitoring systems.

Keywords Pressure detection · Flexible · Textile · Healthcare monitoring

1 Introduction

Reliable, timely, and remote healthcare monitoring improves health outcomes and optimizes resource utilization to meet the urgent needs of an aging population [1–3]. Key parameters, particularly pressure and position, are critical for measuring various body signals, including blood pressure, respiration rate, and gait, and to support clinical judgment and effective management [4–6]. One promising solution to monitor these parameters is the integration of healthcare devices into textiles [7, 8]. The effectiveness of this approach depends on sensor performance, including sensor sensitivity, pressure detection range, reliability, and textile properties [9, 10]. It is essential to align the specific application with sensor performance to ensure reliable and efficient measurements.

In health monitoring, the pressure detection range varies depending on the specific stimulus and body parts being measured. Intra-body pressure, such as intraocular pressure and intracranial pressure, typically falls below 10 kPa. In contrast, the medium pressure regime ranges from 10 to 100 kPa, encompassing heartbeat and blood pressure measurements. In addition, the plantar pressure exceeds 100 kPa [11, 12]. Ongoing research in structural and material engineering focuses on enhancing sensor performance, particularly sensitivity and detection range to meet the demands of wearable technologies[13–15]. However, using a single type of sensor to meet the varied needs of these applications remains challenging. A sensor optimized for pulse measurement may lack the pressure range and linearity for external pressure measurement, such as plantar pressure [16–19]. Developing high-sensitivity sensors with wide detection ranges is resource-intensive, particularly when only specific pressure ranges are needed. This underscores the need for pressure detection devices with tunable pressure ranges. By

✉ Xiaoming Tao
xiao-ming.tao@polyu.edu.hk

1 School of Fashion and Textiles, The Hong Kong Polytechnic University, Hung Hom, Kowloon 999077, Hong Kong SAR, China

2 Research Institute for Intelligent Wearable Systems, The Hong Kong Polytechnic University, Hung Hom, Kowloon 999077, Hong Kong SAR, China

adopting customizable designs, performance can be optimized for specific applications, balancing performance and practicality.

To overcome these challenges, emulating human skin offers an innovative pathway. Human skin contains various mechanoreceptors positioned strategically to detect pressure and other mechanical changes [20–22]. The mechanoreceptors can be broadly categorized into low-threshold mechanoreceptors, like Merkel disks and Meissner's corpuscles, for light, benign pressure (0.07–5 mN), and high-threshold mechanoreceptors, like nociceptive neurons, for stronger, harmful pressure [23, 24]. After activation, these mechanoreceptors generate action potentials (spike signals), which are transmitted via synapses to the brain [25]. The brain analyses the signal to determine the location and pressure. Although the skin does not detect precise pressure, it effectively recognizes change in pressure, offering protection and valuable information. Customizing sensor performance for specific pressure ranges is emerging as a practical approach to effectively and efficiently detect pressure for health monitoring. A customized pressure-sensitive resistor has been designed for clinics, allowing pressure thresholds to be set at 12 levels within the range of 4.9 kPa to 7.1 MPa [26]. This advancement can enhance energy efficiency and measurement reliability. However, further improvements are required in its flexibility, durability, and pressure detection range controllability. In addition, monolithic pressure sensors struggle to effectively perceive the two-dimensional distribution of pressure, limiting their further applications.

Consequently, research on arrayed skin mechanoreceptors that can detect touch and pressure in multidimensional spaces has gradually emerged and has been successively reported. For example, a novel three-dimensional structure mimicking the spatial arrangement of mechanoreceptive corpuscles in human skin has been developed, achieving highly sensitive identification and differentiation of pressure, shear force, and strain as well as their directions [27]. In addition, a skin-mimetic electronic device emulating slow-adapting mechanoreceptors in human skin has been designed, enabling the decoupling of pressure, shear force, and strain [28]. An innovative approach has involved fusing the feature perception and parsing separation [29, 30]; however, a decoding method is still needed to decouple pressure and mapping information. Despite these advancements, existing arrayed devices pose higher demands in terms of structure, wiring, algorithms, data analysis, and system design. Therefore, overcoming the systemic complexity of arrayed devices and ensuring their efficient and stable operation in practical applications is still a significant challenge.

In this study, we propose a novel mechanoreceptor, that incorporates polydimethylsiloxane (PDMS) structures inside the insulation layer to control its pressure initiation threshold. This design achieves an impressive 10^{-8} on–off ratio. By employing structural and material engineering, the pressure threshold of the mechanoreceptor has been tuned in the range of 1.94 kPa to 15 MPa. This tuning is achieved by adjusting several parameters, including the material filling rate, height of the structure, elastomer hardness, composite fabric types, compression area, and the mechanoreceptor sizes. This versatility allows us to tailor the mechanoreceptor's performance to meet specific application requirements, expanding its potential application. This design also ensures the device maintains good durability under repeated compressions (40,000 cycles) and withstands 20 washes. Moreover, a mechanoreceptor array has been developed to map the pressing position, which fuses the pressure detection and parsing separation. The array operates with only two output channels for energy and data processing, simplifying the system and saving time and energy during data processing. This array demonstrates reliable performance in different environments, showing great potential for healthcare monitoring. We finally present three prototypes, including sensor stimulation for children and elderly, and fall detection for Parkinson's patients, to demonstrate the potential of the mechanoreceptor and its array.

2 Results

2.1 Design Concept and Principle of the Mechanoreceptors

To design a customized and controllable mechanoreceptor for various applications, it is crucial to engineer its structure in determining the tunability of the pressure threshold. In line with this objective, Fig. 1a presents an innovative exploded view of the mechanoreceptor's structure, which consists of six distinct layers. The outermost layer is composed of composite fabrics, followed by an electrode layer. At the center, there is a thermoplastic polyurethane (TPU) layer that contains a cavity filled with PDMS structure. The PDMS structures serve as the core of the mechanoreceptor, playing a vital role in controlling its pressure threshold. The presence of the PDMS structures endows the mechanoreceptor with a good on–off resistance ratio. The on–off resistance of this pressure mechanoreceptor is shown in Fig. 1b and c. The off-state resistance is around 360 MΩ, while the on-state resistance, measured with a multimeter, is approximately 2.0 Ω (Fig. 1c and Supplementary Video 1). Through calculation, the on–off resistance difference of the pressure mechanoreceptors is around eight orders of magnitude, comparable to commercial mechanoreceptors. This high on–off response ensures signal fidelity and reliability.

The major technique used in the assembly of textile-based mechanoreceptor is hot-pressing, also known as hot lamination. It is a mature and facile technique that

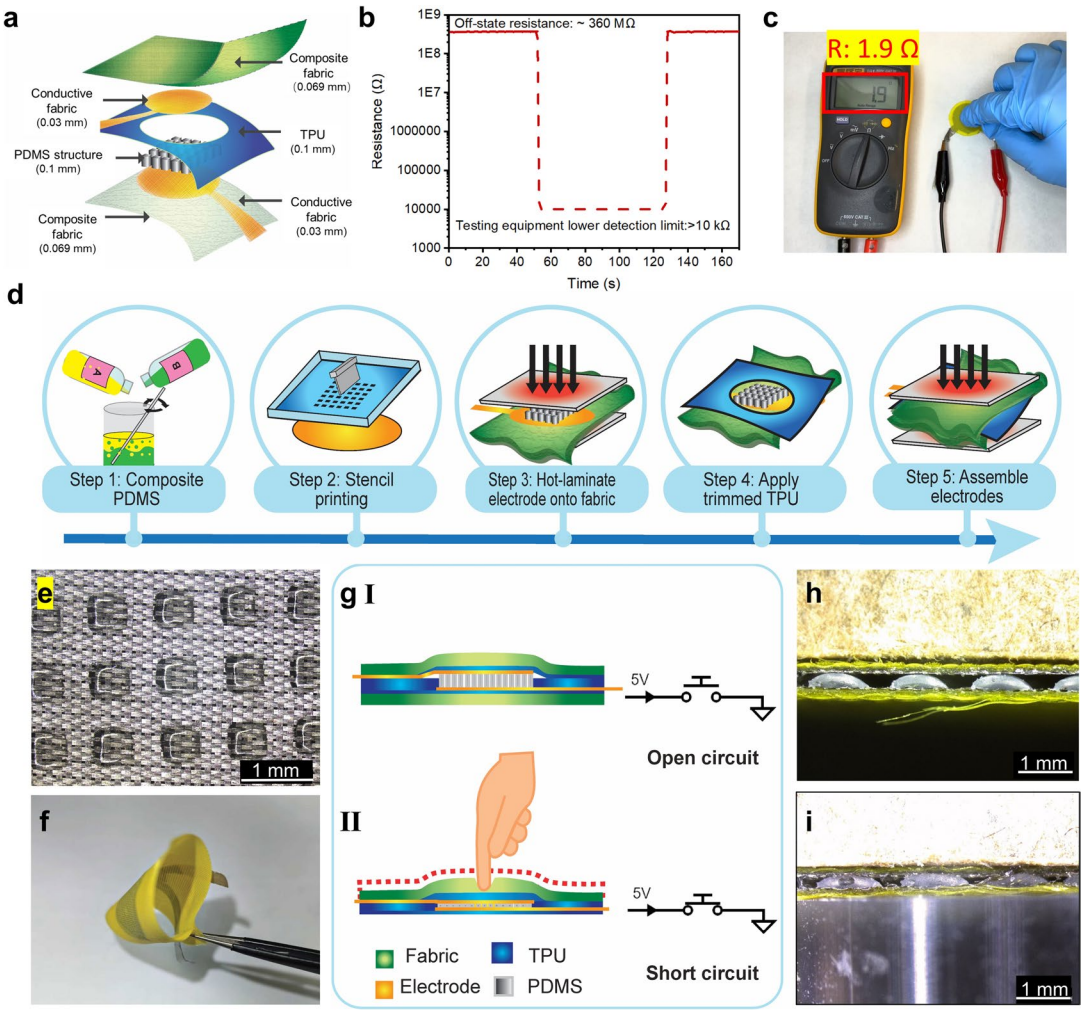

Fig. 1 Design, fabrication and mechanism of the mechanoreceptor. **a** Exploded-view schematic diagram of the mechanoreceptor structure. **b** Measurement of the mechanoreceptor's on–off resistance using an insulation resistance meter. **c** Photograph showing the off-state resistance of the mechanoreceptor. **d** Schematic illustrating the fabrication process of the mechanoreceptor. **e** Optical image of the stencil-printed PDMS structure. **f** Photograph showing the flexibility of the mechanoreceptor. **g** Schematic diagram of the mechanoreceptor mechanism: (I) unloaded state; (II) loaded state. **h** Cross-sectional optical image of the mechanoreceptor in the unloaded state. **i** Cross-sectional optical image of the mechanoreceptor under loading

assembles textiles with other functional materials with strong adhesion. Figure 1d illustrates the fabrication process of the mechanoreceptor. After stencil-printing, the dimensions of the elastomer pillars are measured using an optical microscope (Fig. 1e). The measured dimension of the structure is 0. 542 mm (standard deviation (SD): 0.016 mm). The actual size is slightly larger than the design (0.5 mm) due to the diffusion of the PDMS during solidification. Hot lamination offers advantage in scalability, cost-effectiveness, and potential for automation, making it feasible to produce the mechanoreceptor on a large scale. The thickness of the textile-based pressure mechanoreceptor is only 0.455 mm, as measured with a thickness gage. The mechanoreceptor features a remarkably thin profile and is integrated into textile materials that exhibit excellent deformability and flexibility, as shown in Fig. 1f.

The study of the mechanoreceptor's mechanism provides valuable insights into its design and functionality. Its mechanism is based on the piezoresistive sensor with architecture microstructures, as illustrated in Fig. 1g. Its functionality arises from the dynamic interaction between PDMS pillars, a TPU spacer, and the conductive fabric. Specifically, the PDMS pillars serve as deformable elastomeric structures that modulate contact under pressure; the TPU spacer maintains a void gap between electrodes, ensuring an open-circuit; the conductive fabrics bridge the gap during compression, forming a closed-circuit. In the off-state (no compression), the upper electrode remains separated from the

lower electrode (Fig. 1g(I)). When compressed, the PDMS pillars expand laterally and shorten axially due to Poisson's effect, progressively reducing the void gap. As compression increases, the PDMS pillars reach a geometric deformation limit constrained by their spacing and material properties, which forces the upper electrode into contact with the lower electrode, thus creating as a closed-circuit (Fig. 1g(II)). Upon pressure release, the PDMS pillars recover to their original shape due to the entropic elasticity of the cross-linked polymer chains. This supported the upper electrode back to its original position, resulting in an open-circuit. The pressure threshold is defined as the minimum compression level required to close the void gap, triggering a significant resistance change. This threshold depends on pillar geometry, material hardness, void size, and others. To validate the operating mechanism, we have conducted a cross-sectional analysis of this textile-based mechanoreceptor (with a 0.3-mm height in PDMS structure) using an optical microscope under loaded and unloaded conditions, as depicted in Fig. 1h and i. The total thickness of the mechanoreceptor without loading is 0.69 mm, while the thickness under loading decreased to 0.423 mm. The PDMS height at the center of the mechanoreceptor is 0.274 mm, while the pillars deform to 0.217 mm under loading. This corresponds to a critical strain of 38.69%. This deformation aligns with the closure of the void gap closure required to bridge the electrodes, directly confirming the strain-dependent transition from the open-circuit ("off-state") to the closed-circuit ("on-state").

2.2 Performance and Characterization of the Textile-Based Mechanoreceptor

To develop energy-efficient and customized mechanoreceptors tailored for specific users and applications, it is essential to ensure that the pressure threshold of the mechanoreceptor is adjustable. The pressure threshold of this novel mechanoreceptor is primarily governed by the PDMS structure, includes factors such as the dimension, height, and hardness of the PDMS material. In addition, other factors, like composite fabric, the compression area, and the size of the mechanoreceptor also significantly influence its pressure threshold. This study comprehensively examines the relationship between these factors and the mechanoreceptor pressure threshold to enhance its practical applications. Figure 2a shows the experimental setup**.**

We have initially focused on the material filling rate, a key parameter influenced by the design of the PDMS structure. To explore this, we have designed and fabricated stencils with PDMS structures featuring varying dimensions and spatial arrangements. The variation in the dimension of the elastomer pillars, density, and material filling rate of the mechanoreceptors are summarized in Fig. S1 and Table S1 (Supporting information). In the test, the height of the elastomers (100 μm) and compression area (10 mm in diameter) are kept constant to isolate their effects. Figure 2b reveals that there is a steady increase in compression threshold as the number of material filling rates increased. The mechanoreceptor with an 11-% material filling shows a pressure threshold of 3.86 kPa. The mechanoreceptor with a 44.4-% material filling rate shows higher pressure threshold of 22.67 kPa. When the material filling rate increases to 66%, the pressure threshold rises to 44.87 kPa. The increase in the material filling rate corresponds to larger dimensions of the PDMS structure and a reduced number of PDMS structures, which enhances the compressibility of the mechanoreceptor. Consequently, the pressure threshold of the mechanoreceptor increases. Figure 2d demonstrates that the mechanoreceptor is activated under 30-g loading in a compression area of 10 mm in diameter (see Supplementary video 2). This demonstrates its sensitivity to pressure.

Further investigation of the structural dimension and the pressure threshold of the mechanoreceptor has shown that the height of the elastomer pillars increases with the pressure threshold. Stencils with a consistent pattern (25-% material filling rate) have been fabricated in varying thicknesses: 100 μm, 150 μm, 200 μm, 250 μm, and 300 μm. The thicknesses of the stencil-printed PDMS structure are summarized in Table S2 (Supporting information). Figure 2c reveals a gradual increase in pressure threshold as the height of the elastomer pillars increases. The pressure threshold of the mechanoreceptor printed with a 100-μm stencil is approximately 7.21 kPa. This increases to 46.22 kPa with a 200-μm stencil, and then sharply increases to 512.37 kPa when a 300-μm stencil is employed. As the height of the elastomer pillars increases, the void between the electrodes also enlarges. The upper electrode needs to pull more downward to contact with the lower electrode. Based on this, the pressure threshold correspondingly increases with the height of the elastomer pillars.

In addition to PDMS structural height, the mechanoreceptor pressure threshold increases with PDMS hardness. Figure 2e outlines the relationship between mechanoreceptor's pressure threshold and the PDMS's Shore hardness. Furthermore, as the outer shell composite fabric becomes thicker and more rigid, the mechanoreceptor pressure threshold increases (Fig. 2f). The bending rigidity of the four composite fabrics is presented in Fig. S2 and Table S3 (Supporting information). The thicknesses of the four composite fabrics are provided in Table S4. As the composite fabric continuous to become stiffer, the mechanoreceptor experiences bending. During testing, the mechanoreceptor undergoes some degree of deformation, which leads to a reduction in its pressure.

Besides factors relating to the design and material engineering of the mechanoreceptor, other factors influence the pressure threshold performance of the mechanoreceptor,

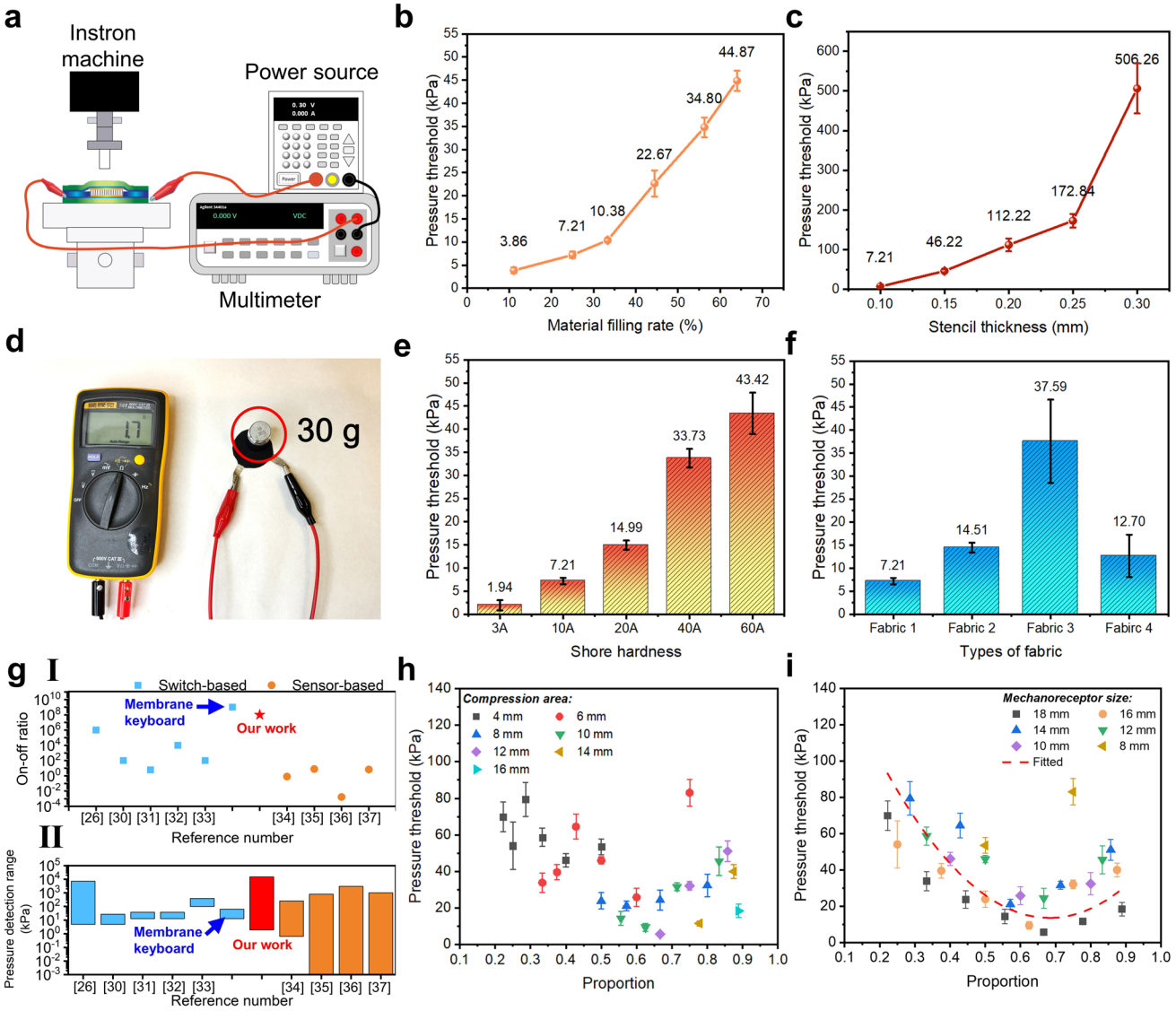

Fig. 2 Tunability of the mechanoreceptor pressure threshold. **a** Schematic diagram of the experimental setup for pressure threshold measurement. **b** Pressure threshold measurement of the mechanoreceptor with various material filling rates (mean ± SD; $n = 3$). **c** Pressure threshold measurement of the mechanoreceptors fabricated using stencils of different thicknesses (mean ± SD; $n = 3$). **d** Photograph showing the mechanoreceptor response under a 30 g load applied over a 10 mm diameter compression area. **e** Pressure threshold measurement of the mechanoreceptor with PDMS of varying hardness (mean ± SD; $n = 3$). **f** Pressure threshold measurement of the mechanoreceptor with different composite fabrics (mean ± SD; $n = 3$). **g** Comparative analysis of the mechanoreceptor with prior pressure detection devices: (I) on–off ratio; (II) pressure detection range. **h** Pressure threshold measurements of the mechanoreceptor with varying sizes, tested under seven different compression areas (mean ± SD; $n = 3$). **i** Pressure threshold measurements of the mechanoreceptor under different compression areas, evaluated across various mechanoreceptor sizes (mean ± SD; $n = 3$)

includes the compression area and the size of the mechanoreceptor (defined by the hole diameter of the voids within it). We have fabricated a series of mechanoreceptors in various sizes (guided by the hole diameter of the TPU spacer), and evaluated their performance under various compression areas. The term "proportion" refers to the ratio between the compression area and the size of the mechanoreceptor, where the size determines the void dimensions. Figure 2h demonstrates the relationship between the mechanoreceptor's pressure threshold and its size across varying compression-to-size ratios. It is observed that the variation of the pressure threshold under a smaller compression area is quite large. Figure 2i demonstrates the relationship between the pressure threshold of the mechanoreceptor and the compression area under varying proportional conditions. As compression area increases for the same size of mechanoreceptor, the pressure threshold first decreases, reaches a lower point, and then begins to increase. This phenomenon can be attributed to

the interaction between PDMS structures, the TPU spacer, and the compression area. Specifically, when the ratio of the compression area to the spacer is either too high or too low, the stress distribution becomes uneven, necessitating increased pressure for activation. Overall, we have conducted a comparative analysis of this novel mechanoreceptor to prior pressure detection device in two aspects—the on–off ratio (Fig. 2g(I)) and the pressure detection range (Fig. 2g(II)) [31–37]. This novel mechanoreceptor shows an advanced on–off ratio, of over eight orders of magnitude, comparable to the commercial rigid product. In addition, the pressure detection range has been adjusted to span over eight orders of magnitude through various combinations. Other performance comparisons with prior works are summarized in Table S5. This adaptability has enabled tailored solutions to meet diverse application needs, enhancing performance and reliability in targeted use cases.

2.3 Other Performance of the Mechanoreceptor

To access the performance of the mechanoreceptor, the material filling rate of 25% is selected, and the compression area is fixed at a circular diameter of 10 mm. Figure 3a shows the response and recovery times of the mechanoreceptor across varying heights of the PDMS structure. As the height of the PDMS structure increases, the response time decreases, whereas the recovery time increases. Mechanoreceptors with lower pressure thresholds require more time to detect smaller pressure change, leading to longer response time. This is attributed to the viscoelastic properties of the PDMS structure. Under low stress, PDMS is dominated by the viscoelastic creep: polymer slowly rearranges and slides, causing time-dependent deformation (creep). Conversely, at higher stress, the PDMS deformation is governed by its elastic component—the cross-linked polymer network. The covalent bond in the network deforms rapidly, enabling faster stabilization of mechanical strain. Figure 3b presents the response time and recovery time of the mechanoreceptor with a thickness of 0.1 mm and a 25-% material filling rate. Its response time is approximately 6 ms and the recovery time is 3.3 ms. This mechanoreceptor demonstrates excellent time performance, making it well-suited for practical applications that require rapid response and recovery times. Besides response time, the frequency response of the mechanoreceptor was evaluated at the frequencies of 0.125 kHz, 0.25 kHz, 0.5 kHz, and 1 kHz. Figure 3c demonstrates that the mechanoreceptor responds to different compression frequencies within the range of typical human biologic signals.

In addition to evaluating time and frequency response, the durability and reliability of the mechanoreceptor in different scenarios have been assessed. A test involving 40,000 compressions at a pressure of 10 kPa was conducted to evaluate the mechanical and electrical properties of the mechanoreceptors. The voltage response of the mechanoreceptor is shown in Fig. 3d. In detail, the voltage response of the mechanoreceptor from 0 to ten cycles and from 39,990 to 40,000 cycles are similar (Fig. 3e and f). The results indicate that the voltage signal remains highly stable and reproducible during 40,000 cycles of compression. However, as depicted in Fig. 3g, the on-state duration at the cycles of 39,551 is shorter than that of the initial, suggesting that repeated compressions may slightly alter the pressure threshold. Despite this, the mechanoreceptor continues to function effectively after 40,000 cycles.

In addition to compression reliability, the on–off resistance of the mechanoreceptors has been measured across 20 washing cycles. Figure 3h demonstrates that off-resistance decreases to 111.97 MΩ after 20 washes, while maintaining a resistance difference spanning 8 orders of magnitude. The value remains above the 20-MΩ threshold specified for unqualified membrane keyboards, refer to GB/T 30091. In addition, the mechanical response of the mechanoreceptor throughout 20 washes has been evaluated (Fig. 3i). After 20 washing cycles, the mechanoreceptor exhibits a deterioration in stability, characterized by a decreased slope in the response curve, indicating a longer response time. In addition, the on-state period of the mechanoreceptor after 20 washing cycles is longer than that of the unwashed mechanoreceptor, implying a reduction in the pressure threshold. Moreover, the signal of the mechanoreceptor shows increased fluctuations after 20 washing cycles.

2.4 Design and Characterization of the Mechanoreceptor Array

To advance multidimensional pressure mapping while simplifying system complexity, we have developed an innovative spiral-shaped array of mechanoreceptors that mimic the pressure sensations of the human body. By establishing a defined threshold in the detection unit, we can filter out noise and prevent unnecessary data decoding. Figure 4a presents an exploded schematic diagram of this mechanoreceptor array, which contains six layers. Specifically, it comprises 16 mechanoreceptors and 16 flexible resistors (~3 kΩ) connected in series. The equivalent circuit is shown in Fig. 4b. This design integrates both mechanoreceptors and resistors in terms of physical space and signal processing. This system employs a dual-channel signal acquisition architecture to achieve two-dimensional pressure sensing via spatially resolved differential analysis. Pressure detection is governed by a tunable threshold filtering mechanism in the mechanoreceptor; where the applied forces exceed a threshold, it triggers a critical resistance drop. Concurrently, position mapping is accomplished through spatially encoded weighted voltage gradients between the dual channels, generated by the spiral array's geometry.

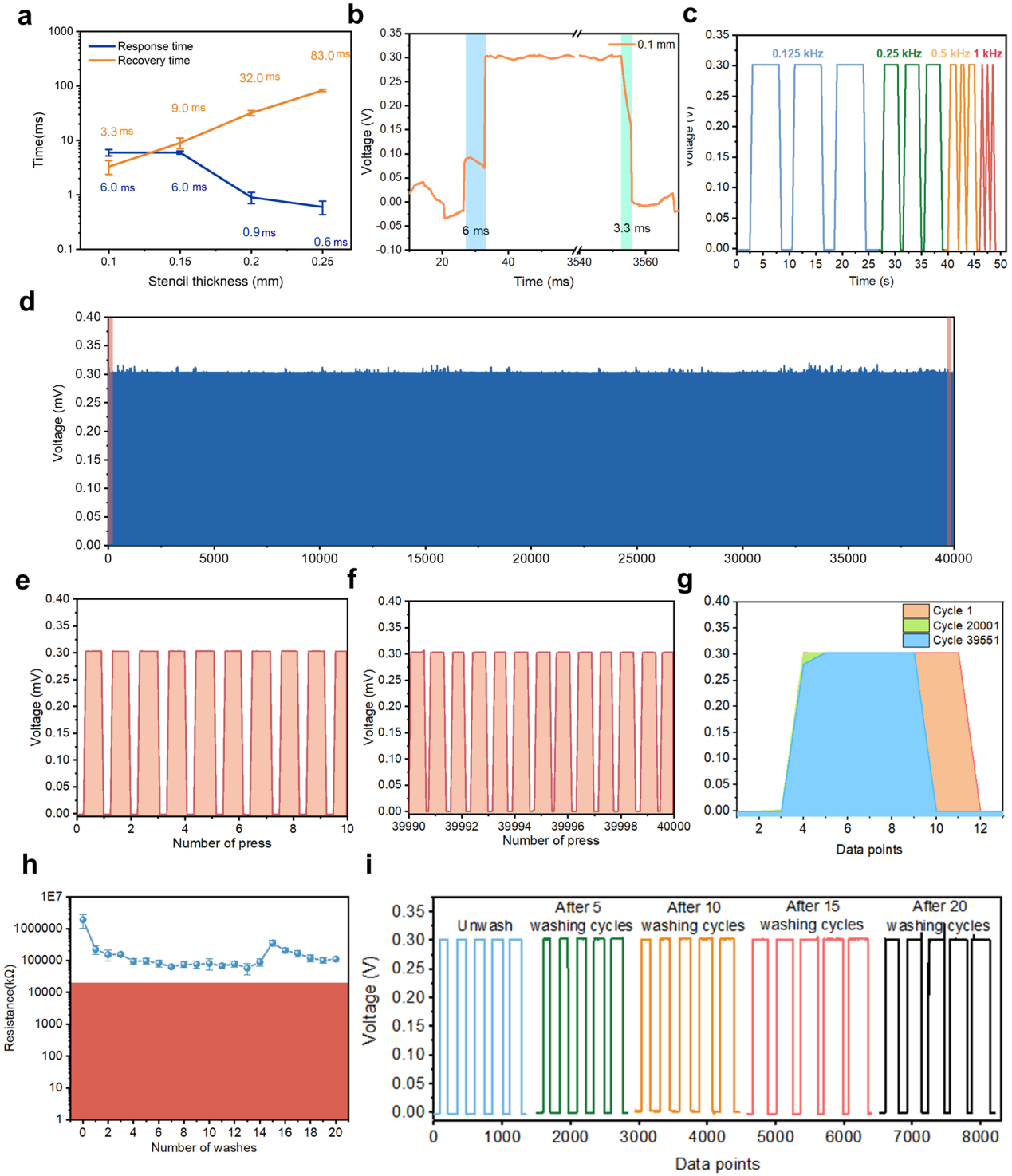

Fig. 3 Characterization of the mechanoreceptor. **a** Response and recovery time measurements of the mechanoreceptor with varying stencil thicknesses (mean ± SD; $n = 3$). **b** Detailed response and recovery time measurements for a mechanoreceptor with a 0.1 mm thickness and 25-% material filling rate. **c** Frequency response measurement of the mechanoreceptor. **d** Stability assessment of the mechanoreceptor through 40,000 loading–unloading cycles. **e** Voltage response characterization during cycles 1–10. **f** Voltage response characterization during cycles 39,990–40,000. **g** Comparative voltage response analysis between cycle 1 and cycle 39,551. **h** Off-state resistance of the mechanoreceptor over 20 wash cycles. **i** Electrical and mechanical performance of the mechanoreceptor across 20 wash cycles

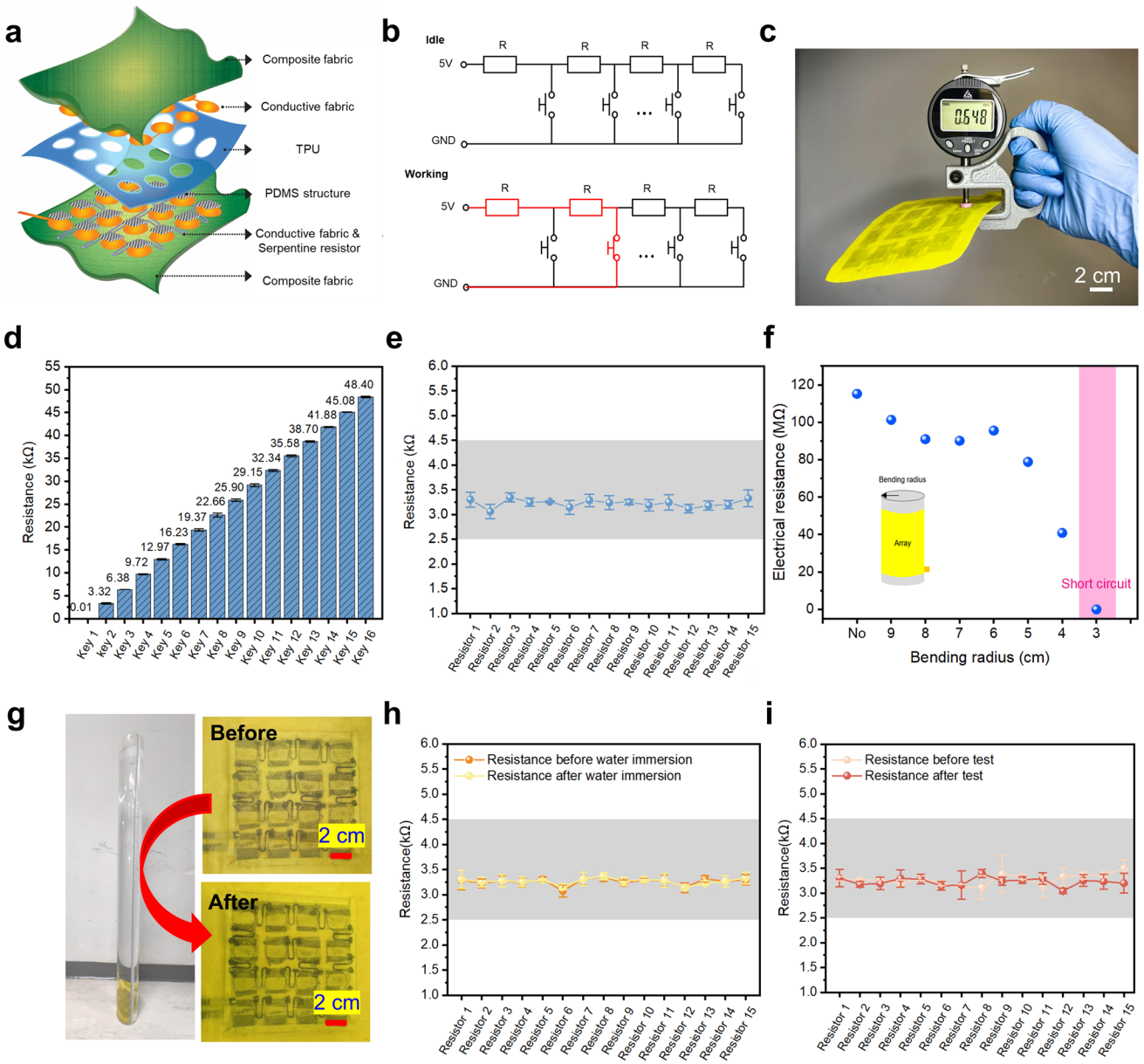

Fig. 4 Design, mechanism and characterization of the mechanoreceptor array. **a** Exploded schematic diagram of the mechanoreceptor array illustrating its structural design. **b** Electric circuit diagram of the array. **c** Photograph depicting the thickness of the mechanoreceptor array. **d** Electrical resistance measurement of the mechanoreceptor array at various positions (mean ± SD; $n = 3$). **e** Electrical resistance difference across different positions within the array (mean ± SD; $n = 3$). **f** Off-state resistance measurement of the array under different bending radii. **g** Photograph comparing the array before and after water-immersion test. **h** Resistance measurement before and after water-immersion test (mean ± SD; $n = 3$). **i** Resistance of the array before and after cyclic temperature test (mean ± SD; $n = 3$)

Three array samples were fabricated, and their thickness are 0.648 mm, as shown in Fig. 4c. The resistance of each individual mechanoreceptor under compression has been measured using a multimeter, as shown in Fig. 4d. There are 16 levels of resistance variations, ranging from 0.01 to 48.4 kΩ. The standard deviation of mechanoreceptor resistance between samples is only around 0.18. The average resistance difference between mechanoreceptors is 3.226 kΩ, as presented in Fig. 4e. The resistance variation among the mechanoreceptors is 0.11 kΩ. The resistance difference between mechanoreceptors is maintained within the range of 2–4.5 kΩ, demonstrating the practical manufacturability of this mechanoreceptor array. Considering the requirements of wearable applications, it is crucial to evaluate the functionality of the mechanoreceptor array under bending. To this end, acrylic tubes with different radii were manufactured to evaluate whether the mechanoreceptor array could maintain an off-state under different bending radii. Figure 4f presents

the off-state resistance of the array while it is bent along its electrodes. The off-state resistance decreases at a bending radius of 4 cm, resulting in a short circuit at a 3-cm radius. In addition, we assess the electrical state of the circuit under different bending radius bending at different directions, as shown in Table S6 (Supporting information). The mechanoreceptor array remains in the off-state with the bending radius of 5 cm along its electrode, while it remains off-state only when bent at 8 cm in a direction perpendicular to the electrode direction. When applying the mechanoreceptor array in practical applications, it is essential to consider the bending radius direction of the device. For textile properties, we have evaluated the whole mechanoreceptor array bending rigidity via the KES system. Due to the load limitation of the system, the mechanoreceptor array has been cut into 10 pieces, each with a width of 1 cm. The total bending load of the mechanoreceptor array is 60. 22 gF (0.588 N), as depicted in Fig. S3 (Supporting information).

2.5 Durability and Reliability of the Mechanoreceptor Array

The durability and reliability of the array are critical factors in wearable applications. We have conducted comprehensive experiments to evaluate these aspects, focusing on water repellence, environmental stability, and mechanical stability. This textile mechanoreceptor exhibits excellent water-repellent properties due to its fabrication, structure, and materials. To evaluate the protection, a water-soluble ink paper with one side red and one side white have been adhered to the edge of the array. After 30 min, we observed no ink exposure and penetration on the surroundings or backside paper (Fig. 4g). This confirms that the TPU spacer used in hot lamination effectively protects the mechanoreceptor underwater. The mechanoreceptor resistance also has been evaluated with a multimeter before and after the test. Figure 4h proves that the resistance of the mechanoreceptor array remains stable after water immersion. The average resistance difference observed was minimal, with values of 3.26 kΩ before the test and 3.27 kΩ after the test. Statistical analysis revealed no significant difference in the mechanoreceptor resistance before and after the water immersion test.

The stability of the mechanoreceptor array in various environments is crucial for practical applications. Three different environmental tests have been conducted to comprehensively evaluate the textile mechanoreceptor array performance, including a high-temperature test, a low-temperature test, and a cyclic temperature test, in accordance with GB/T 30091. The off-state resistance of the mechanoreceptor array before the cyclic temperature test is 276.80 MΩ. After the test, the off resistance of the mechanoreceptor is 398.8 MΩ (Table S7). There is no significant difference in off-resistance during the cyclic temperature test. Figure 4i evaluates the mechanoreceptor resistance before and after the cyclic temperature test, and Fig. S4 shows the resistance difference between individual keys. The resistance of each mechanoreceptor remains stable throughout the test. The off resistance of the mechanoreceptor array before and after the high-temperature tests is 365.42 MΩ and 266.2 MΩ, as detailed in Table S8 (Supporting information). There is no significant difference in the mechanoreceptor resistance in the pair t test. The on-state resistance of each mechanoreceptor before and after the test is also similar, as shown in Fig. S5 (Supporting information). For the low-temperature tests, the off resistance of the mechanoreceptor array before and after the tests are 450.46 MΩ and 125.25 MΩ, listed out in Table S9. It decreases by approximately 72.17%, while its resistance remains above the required qualification threshold of 20 MΩ. Despite this change in off-state resistance, the on-state resistance of each mechanoreceptor does not show significant differences before and after the test, which is summarized in Fig. S6 (Supporting information). Overall, these experiments confirm the textile mechanoreceptor array stability across various environmental conditions.

In addition, the off-state resistance of the array has been measured over time to evaluate its stability. Figure S7 demonstrates the resistance variation along time, from 1 to 100,000 min. The average resistance between keys at initial is 3.22 kΩ, which increases to 3.33 kΩ after 100,000 min, as shown in Fig. S8 (Supporting information). The resistance of each keys slightly increases by around 3.4% after 10,000 min. The resistance between keys remains within the range of 2.5–4.5 kΩ. Since the resistance variation stacks along the series, we outline four key resistance variations along time in Fig. S9a, S9b, S9c, and S9d. It has been observed that the resistance of mechanoreceptor 8 is slightly over the detection range. The resistance of Key 12 and Key 16 at 10,000 min exceeds the range slightly. This is attributed to the connection between the resistor and the mechanoreceptor, which required further improvement.

In addition to evaluating longevity, the mechanical stability of the textile mechanoreceptor array under load has been tested. According to GB/T 30091-2013, the off resistance of the mechanoreceptor array must meet the 20-MΩ requirement. Detailed information is shown in Fig. S10 (Supporting information). In addition, the on-state resistance of the array under different users pressing has been assessed, as presented in Fig. S11 (Supporting information). These comprehensive evaluations confirm the mechanoreceptor array's reliability and adaptability for diverse practical applications.

3 Applications

Health is a holistic concept that encompasses physical, mental, and social well-being. In recent years, the emergence of innovative wearable electronics technology has significantly increased awareness around personal healthcare management. Individuals are increasingly proactive in taking responsibility for managing their health and that of their family members. This shift has led to a growing demand for various types of flexible healthcare devices, offering distinct functionalities for different applications. In response to this demand, we have developed three different types of flexible healthcare devices, tailored for various users and applications, to explore the potential of the mechanoreceptors and the array.

Sensory stimulation is a widely used intervention that presents various stimulus to engage different sensory modalities, including hearing, touching, vision, and smelling [38]. These approaches enhance the well-being of various groups, like the elderly and children. In the context of children, sensory stimulation effectively links to fine motor skill training [39]. Fine motor skills involves small and precise movement with hands, fingers, and toes require coordination, muscle strength, sensation, dexterity, and awareness [40]. Developing fine motor skills offers several advantages for children, including enhanced independence, improved hand–eye coordination, increased concentration and enhanced cognitive development [41, 42]. There are various training activities for children to train their motor skills, like finger painting and puzzling [43]. However, these activities face challenges, like limited engagement, insufficient feedback, and a lack of adaptability. By incorporating tactile and visual stimuli into activities, children can experience enhanced engagement and receive more comprehensive feedback. This has the potential to improve their hand–eye coordination, dexterity, and precision.

In response to the need of interactive learning tools, we have developed an interactive sensory book that integrates visual and tactile stimuli to help children learn and identify shapes, as illustrated in Fig. 5a. This interactive sensory book comprises a mechanoreceptor array with 16 mechanoreceptors in connection with an Arduino Due board, which interfaces with an LED display. Figure 5b shows the system architecture. When pressure is applied to the target position, the microcontroller measures the resulting resistance to identify the corresponding image. The sensory book demonstrates excellent flexibility and deformability, as shown in Fig. 5c. In particular, Fig. 5c(I), (II), (III), and (IV) shows the interaction of the sensory book when the pressure is applied at different positions, corresponding to Key 1, Key 5, and Key 15. It proves the functionality of the mechanoreceptor. Additional interactions are shown in Supplementary Video 3, highlighting the book's capabilities. Engaging with the book requires children to manipulate and explore different textures and shapes, an activity that enhances dexterity and hand–eye coordination. Previous research underscores the connection between fine motor skills and cognitive development, demonstrating that such activities can promote holistic cognitive advancement [44, 45].

As the global population ages, the challenges of cognitive decline and dementia have become public health concerns. Sensory stimulation has emerged as a popular approach to alleviate the symptoms of dementia [46]. Visual stimuli activate the visual processing function of the elderly to lessen the decline [47, 48]. In addition, the elderly often faces challenges with hand strength and dexterity, especially in precise controlling of hand pressure for complicated tasks. To address these challenges, a tactile visual memory tool also has been customized as a training tool for the elderly to meet the challenges of dementia to improve their life quality [49–52]. Figure 5d illustrates the training protocol: the display first generates a sequence of numbers for a few seconds to allow the elderly to memorize it. After this, the user needs to input the sequence by pressing the corresponding numbers of the array. This improves the short-term memory in the elderly and encourages cognitive engagement. Figure 5h(I), (II), (III) and (IV) illustrates the functionality of the tool, demonstrating the response of the tool when different numbers are pressed. A full demonstration is provided in the Supplementary Video 4.

Parkinson's disease encompasses a group of neurologic disorders characterized by movement problems or other neurodegenerative diseases, such as rigidity, slowness, tremors, and progressive supranuclear palsy [53]. A significant risk for individuals with Parkinson's disease is the increased likelihood of falls. Statistics show that 38% of patients with Parkinson's disease fall, and 13% fall more than once weekly [54]. Prompt assistance from caregivers is crucial when a fall occurs to prevent serious injury or death. To address this issue, developing a system to measure gait in Parkinson's patients can help mitigate risks [55, 56]. Prior clinical trials have validated that such systems enhance the quality of life by providing real-time feedback for self-correction of gait patterns, reducing fall frequency, and facilitating personalized rehabilitation protocols tailored to individual motor fluctuations [56–58]. Figure 6a outlines the system architecture, containing two mechanoreceptor arrays as input devices connecting to the Arduino board, and an LED or buzzer serving as output. Figure 6c illustrates the system mechanism. When neither of the user's feet contacts the ground, both mechanoreceptor arrays remain inactive, triggering the LED or buzzer to alert the caregiver. The pressure threshold of the mechanoreceptor has been tested, as shown in Fig. 6b. Figure 6d(I), (II), (III), and (IV) shows the system's response

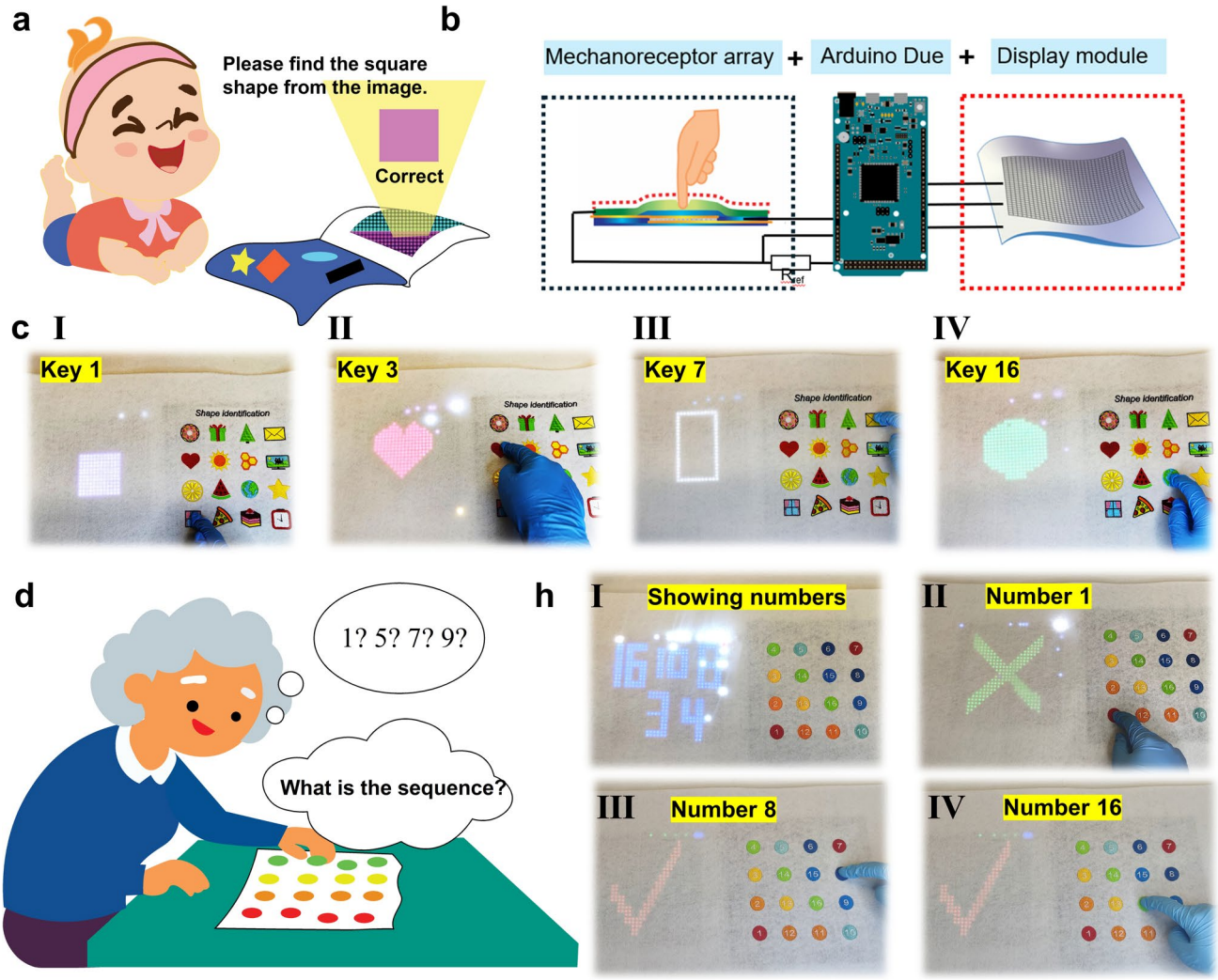

Fig. 5 Mechanoreceptor array for sensory stimulation applications. **a** Illustration of a child using the mechanoreceptor array to learn and identify various shapes via visual feedback. **b** System architecture diagram. **c** Display response to pressure applied at different positions. (I) Key 1. (II) Key 3. (III) Key 7. (IV) Key 16. **d** Illustration showing the application of the mechanoreceptor array for memory training in the elderly, highlighting its potential for cognitive enhancement. **h** (I) Image showing the display generating the number sequences. (II–IV) Display responses when specific numbers are pressed. (II) Number 1. (III) Number 8. (IV) Number 16

under different scenarios, demonstrating the functionality of the fall detection system. A full demonstration is provided in Supplementary Video 5.

4 Conclusions

In this paper, we report a novel mechanoreceptor with a tunable pressure threshold, fabricated via stencil printing and hot lamination techniques of textile materials. A key feature of this design is the incorporation of the PDMS structures within the void of the mechanoreceptor. The pressure threshold of the mechanoreceptor can be controlled across a range of 1.94 kPa to 15 MPa, meeting the requirements for wearable applications and even extending to robotic applications. This architected structure allows control over the pressure threshold of the mechanoreceptor through various parameters, including the material filling rate, the height of the structure, PDMS modulus, types of composite fabrics, compression area and the size of the mechanoreceptor. By exploring the synergistic effects of multiple dimensions, we enhance the design freedom and customization of the mechanoreceptor, avoiding limitations associated with specific parameters. The PDMS structure within the mechanoreceptor's void results in an on–off ratio spanning over eight orders of magnitudes. In addition, the mechanoreceptor exhibits good reliability in repeated compressions (40,000 cycles) and laundering

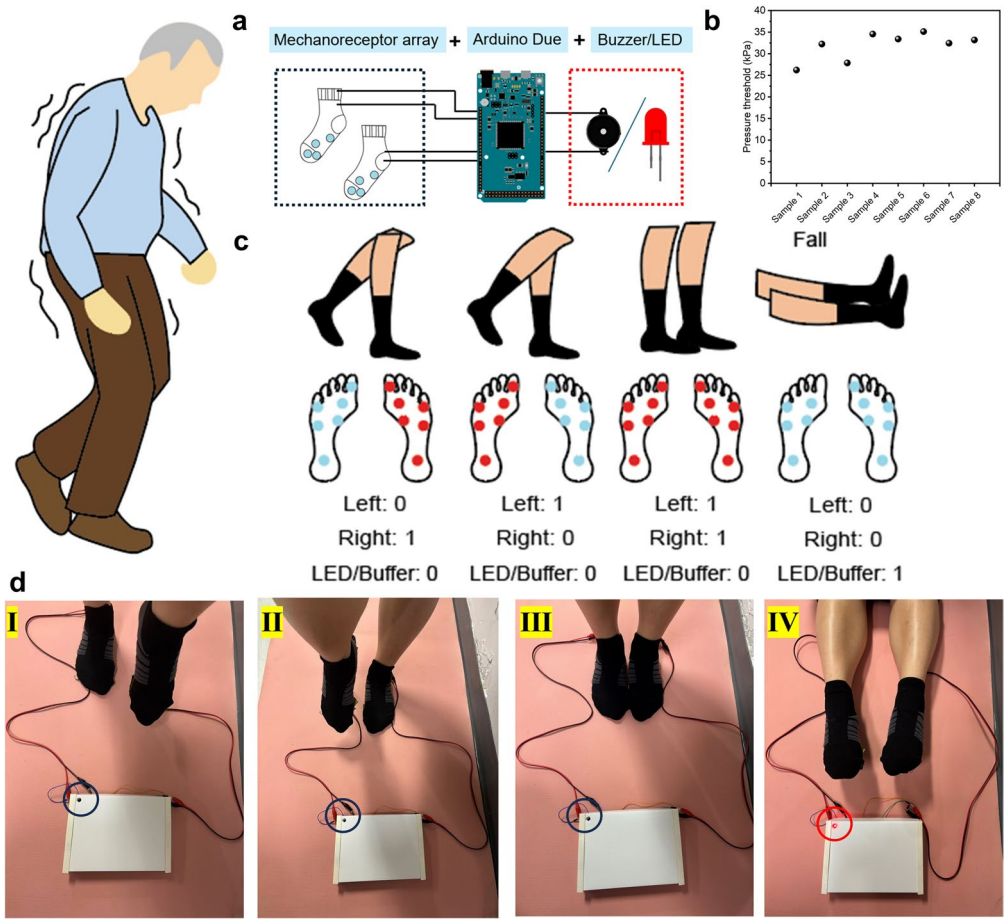

Fig. 6 Fall detection for Parkinson patients. **a** System architecture of the fall detection system. **b** Measurement of the mechanoreceptors pressure threshold. **c** Operational mechanism of the fall detection system. **d** Photograph showing the system response to foot positioning: (I) Right foot lifted; (II) left foot lifted; (III) both feet grounded; (IV) both feet lifted (circles indicate the LED positions)

(20 washes), highlighting its robustness and suitability for practical applications.

In addition, we have designed a spiral-shaped array of mechanoreceptors that enables two-dimensional pressure sensing through an innovative, series–parallel circuit design. By implementing a differential algorithm with dual-output channels, we significantly reduce system complexity while maintaining high-resolution sensing capabilities. The array also exhibits stable performance in various environments, including low-temperature, high-temperature, cyclic temperature, immersion in 1 m of water, pressing by different users, and enduring a mechanical load of 100 N. In response to the growing demand for healthcare devices, we have developed three various prototypes for different healthcare monitoring. These prototypes effectively monitor various body vitals, such as finger pressure, plantar pressure, and gait, demonstrating the mechanoreceptor's customization potential for diverse health-monitoring needs. While these developments highlight the array pressure detection and data processing capability, it is limited to single-point compression. Addressing this limit in further research can solidify its potential, paving the way for more advanced functionality in healthcare applications.

5 Experimental Section

Fabrication of mechanoreceptors: The dimension and the quantity of the elastomer pillars were designed in advance to produce the corresponding stencil (100 μm in thickness) by UV laser cutting. PDMS (Dragon skin 10) was composited in the proportion of 1:1, and waited around 10 min to reach desired viscosity for stencil printing. The elastomer was printed onto the nickel–copper-plated conductive fabric with the corresponding stencil. The electrode thickness was 30 μm and its resistance was 0.03–0.05 Ω/m^2. Following the printing process, a solidification was conducted to stabilize the shape of the elastomer pillars. The electrode with pillars and the pure electrode were then heat-pressed onto separated

laminated fabric at 120 ℃ for 3 s. A TPU spacer with a thickness of 100 μm was prepared by cutting out a 16-mm diameter hole. The spacer was then applied between two laminated electrodes. The whole set was finally hot-pressed at 85 ℃ for 2 s, in which the upper and lower electrode was bonded together via the TPU spacer. In addition, the stencil thickness and types of PDMS used in fabrication were varied, which significantly affected the controllability of the stencil printing and lamination, particularly influencing the viscosity and solidification time.

Characterization of the mechanoreceptor: The thickness of both the materials and mechanoreceptor was measured using a thickness gage. The on–off resistance of the mechanoreceptor was assessed with an RK2681N insulation resistance tester from Shenzhen Meiruike Electronic Technology Co. and a multimeter. The insulation resistance tester had a lower limit of 10 kΩ, while the multimeter upper limit was 120 MΩ. The mechanical performance of the mechanoreceptor was evaluated using an Instron 5566 in compression mode. The setup included a power source and an Agilent 34001a multimeter to measure the mechanoreceptor response under mechanical stress. The response time and recovery time of the mechanoreceptor under various parameters were tested using Instron 5566 and Keysight 4600a. For durability assessment, a laundry test was conducted using a commercial laundry machine, following the AATCC 135 standard. This involved using 66g AATCC 1993 standard reference detergent and 1.8-kg laundering ballast pieces.

Fabrication of the mechanoreceptor array: Conductive graphene/carbon black TPU was laser cut into serpentine shape to serve as a flexible resistor. Each resistor resistance was around 3.36 kΩ measured by a multimeter. Following the established mechanoreceptor fabrication process, elastomer pillars were stencil-printed onto the electrode. Next, the electrode and flexible resistor were hot-pressed onto the composite fabric. The resistor was then in connection with the mechanoreceptor electrode with a conductive tape from 3M Electronic. Finally, a TPU spacer with 16 holes (16 mm in diameter), was laminated between the electrodes to assemble the configuration. In addition, the array sides were laminated with a TPU spacer for encapsulation.

Characterization of the mechanoreceptor array: The on–off resistance of the mechanoreceptor array was measured using an RK2681N insulation resistance tester from Shenzhen Meiruike Electronic Technology Co. and a multimeter. The water-encapsulant properties of the array were tested according to the standard IEC 60529. The highest protection level IPX7 was selected. In the test, the mechanoreceptor arrays were submerged in water at a depth of 1 m for 30 min. A water-soluble ink paper was adhered inside the array. If there is any water penetration, the color of the fabric changes to red. For the cyclic temperature test, the arrays were subjected to alternatively conditions of 55 ℃ (oven) and − 40 ℃ (ESPEC PL-3KPH), each lasting for 30 min, for a total of 5 cycles. The environmental transition time was maintained at less than 3 min. For the low-temperature and high-temperature tests, samples were maintained at − 40 °C and 50 °C for 72 h each.

Supplementary Information The online version contains supplementary material available at https://doi.org/10.1007/s42765-025-00572-3.

Acknowledgements The research has been supported by Research Grants Council of Hong Kong (Grant No. T42-513/24-R), Innovation and Technology Fund (Grant No. MRP/020/21) and The Hong Kong Polytechnic University (Grant No. 847A). Ma acknowledges a postgraduate scholarship from The Hong Kong Polytechnic University.

Funding Open access funding provided by The Hong Kong Polytechnic University.

Data Availability All data Supplementary this study's findings are included in the paper and the Supplementary Information. Additional data related to this paper are available from the corresponding author upon reasonable request.

Declarations

Conflict of interest The Hong Kong Polytechnic University has filed provisional patent applications for the mechanoreceptor and its array.

References

1. Iqbal SMA, Mahgoub I, Du E, Leavitt MA, Asghar W. Advances in healthcare wearable devices. *npj Flex Electron*. **2021**;*5*:9.
2. Lyu Q, Gong S, Yin J, Dyson JM, Cheng W. Soft wearable healthcare materials and devices. *Adv Healthc Mater*. **2021**;*10*:e2100577.
3. Takei K, Honda W, Harada S, Arie T, Akita S. Toward flexible and wearable human-interactive health-monitoring devices. *Adv Healthc Mater*. **2015**;*4*:487.
4. Chen S, Wu N, Ma L, Lin S, Yuan F, Xu Z, Li W, Wang B, Zhou J. Noncontact heartbeat and respiration monitoring based on a hollow microstructured self-powered pressure sensor. *ACS Appl Mater Interfaces*. **2018**;*10*:3660.
5. Khan Y, Ostfeld AE, Lochner CM, Pierre A, Arias AC. Monitoring of vital signs with flexible and wearable medical devices. *Adv Mater*. **2016**;*28*:4373.
6. Mahato K, Saha T, Ding SC, Sandhu SS, Chang AY, Wang JS. Hybrid multimodal wearable sensors for comprehensive health monitoring. *Nat Electron*. **2024**;*7*:735.

7. Shi J, Liu S, Zhang L, Yang B, Shu L, Yang Y, Ren M, Wang Y, Chen J, Chen W, Chai Y, Tao X. Smart textile-integrated microelectronic systems for wearable applications. *Adv Mater*. **2020**;*32*: e1901958.
8. Libanori A, Chen GR, Zhao X, Zhou YH, Chen J. Smart textiles for personalized healthcare. *Nat Electron*. **2022**;*5*:142.
9. Luo Y, Abidian MR, Ahn JH, Akinwande D, Andrews AM, Antonietti M, Bao Z, Berggren M, Berkey CA, Bettinger CJ et al. Technology roadmap for flexible sensors. *ACS Nano*. **2023**;*17*:5211.
10. Wang X, Liu Z, Zhang T. Flexible sensing electronics for wearable/attachable health monitoring. *Small*. **2017**;*13*:1602790.
11. Zang YP, Zhang FJ, Di CA, Zhu DB. Advances of flexible pressure sensors toward artificial intelligence and health care applications. *Mater Horiz*. **2015**;*2*:140.
12. Trung TQ, Lee NE. Flexible and stretchable physical sensor integrated platforms for wearable human-activity monitoringand personal healthcare. *Adv Mater*. **2016**;*28*:4338.
13. Ruth SRA, Feig VR, Tran H, Bao ZN. microengineering pressure sensor active layers for improved performance. *Adv Funct Mater*. **2020**;*30*:2003491.
14. Shi J, Wang L, Dai Z, Zhao L, Du M, Li H, Fang Y. Multiscale hierarchical design of a flexible piezoresistive pressure sensor with high sensitivity and wide linearity range. *Small*. **2018**;*14*: e1800819.
15. Li Y, Zhang W, Zhao C, Li W, Dong E, Xu M, Huang H, Yang Y, Li L, Zheng L, Mao M, Yao S, Wang L, Ma J, Wang X, Huang W. Breaking the saturation of sensitivity for ultrawide range flexible pressure sensors by soft-strain effect. *Adv Mater*. **2024**;*36*: e2405405.
16. He J, Xiao P, Lu W, Shi JW, Zhang L, Liang Y, Pan CF, Kuo SW, Chen T. A universal high accuracy wearable pulse monitoring system via high sensitivity and large linearity graphene pressure sensor. *Nano Energy*. **2019**;*59*:422.
17. Cai Y, Shen J, Yang C-W, Wan Y, Tang H-L, Aljarb AA, Chen C, Fu J-H, Wei X, Huang K-W. Mixed-dimensional MXene-hydrogel heterostructures for electronic skin sensors with ultrabroad working range. *Sci Adv*. **2020**;*6*:eabb5367.
18. Zhai W, Zhu J, Wang Z, Zhao Y, Zhan P, Wang S, Zheng G, Shao C, Dai K, Liu C, Shen C. Stretchable, sensitive strain sensors with a wide workable range and low detection limit for wearable electronic skins. *ACS Appl Mater Interfaces*. **2022**;*14*:4562.
19. Lee J, Shin S, Lee S, Song J, Kang S, Han H, Kim S, Kim S, Seo J, Kim D. Highly sensitive multifilament fiber strain sensors with ultrabroad sensing range for textile electronics. *ACS Nano*. **2018**;*12*:4259.
20. Dargahi J, Najarian S. Human tactile perception as a standard for artificial tactile sensing—a review. *Int J Med Robot*. **2004**;*1*:23.
21. Lee Y, Park J, Choe A, Cho S, Kim J, Ko H. Mimicking human and biological skins for multifunctional skin electronics. *Adv Funct Mater*. **2020**;*30*:1904523.
22. Chortos A, Liu J, Bao Z. Pursuing prosthetic electronic skin. *Nat Mater*. **2016**;*15*:937.
23. Li L, Rutlin M, Abraira VE, Cassidy C, Kus L, Gong S, Jankowski MP, Luo W, Heintz N, Koerber HR. The functional organization of cutaneous low-threshold mechanosensory neurons. *Cell*. **2011**;*147*:1615.
24. Johansson R, Vallbo Å, Westling G. Thresholds of mechanosensitive afferents in the human hand as measured with von Frey hairs. *Brain Res*. **1980**;*184*:343.
25. Abraira VE, Ginty DD. The sensory neurons of touch. *Neuron*. **2013**;*79*:618.
26. Ju B, Kim I, Li BM, Knowles CG, Mills A, Grace L, Jur JS. Inkjet printed textile force sensitive resistors for wearable and healthcare devices. *Adv Healthc Mater*. **2021**;*10*: e2100893.
27. Zeng X, Liu Y, Liu F, Wang W, Liu X, Wei X, Hu Y. A bioinspired three-dimensional integrated e-skin for multiple mechanical stimuli recognition. *Nano Energy*. **2022**;*92*: 106777.
28. Liu Z, Hu X, Bo R, Yang Y, Cheng X, Pang W, Liu Q, Wang Y, Wang S, Xu S. A three-dimensionally architected electronic skin mimicking human mechanosensation. *Science*. **2024**;*384*:987.
29. Huang Z, Yu S, Xu Y, Cao Z, Zhang J, Guo Z, Wu T, Liao Q, Zheng Y, Chen Z, Liao X. In-sensor tactile fusion and logic for accurate intention recognition. *Adv Mater*. **2024**;*36*: e2407329.
30. Xu YJ, Yu SF, Liu L, Lin WS, Cao ZC, Hu Y, Duan JM, Huang ZJ, Wei C, Guo ZQ, Wu TZ, Chen Z, Liao QL, Zheng YJ, Liao XQ. In-sensor touch analysis for intent recognition. *Adv Func Mater*. **2024**;*34*:2411331.
31. Chen M, Xu L, Liu Y, Yu M, Li Y, Ye TT. An all-fabric tactile-sensing keypad with uni-modal and ultrafast response/recovery time for smart clothing applications. *ACS Appl Mater Interfaces*. **2022**;*14*:24946.
32. Shi X, Zuo Y, Zhai P, Shen J, Yang Y, Gao Z, Liao M, Wu J, Wang J, Xu X, Tong Q, Zhang B, Wang B, Sun X, Zhang L, Pei Q, Jin D, Chen P, Peng H. Large-area display textiles integrated with functional systems. *Nature*. **2021**;*591*:240.
33. Zhang YZ, Zou JJ, Wang HJ, Zhou C, Chen XZ. A single-layer less-wires stretchable wearable keyboard based on pressure switch conductive textile. *Smart Mater Struct*. **2022**;*31*: 105008.
34. Zhao J, Preechayasomboon P, Christensen T, Memar AH, Shen Z, Colonnese N, Khbeis M, Zhu M, editors. TouchpadAnyWear: textile-integrated tactile sensors for multimodal high spatial-resolution touch inputs with motion artifacts tolerance. In: Proceedings of the 37th annual ACM symposium on user interface software and technology. **2024**.
35. Lin W, Wang B, Peng G, Shan Y, Hu H, Yang Z. Skin-inspired piezoelectric tactile sensor array with crosstalk-free row+column electrodes for spatiotemporally distinguishing diverse stimuli. *Adv Sci (Weinh)*. **2021**;*8*:2002817.
36. Jang J, Oh B, Jo S, Park S, An HS, Lee S, Cheong WH, Yoo S, Park JU. Human-interactive, active-matrix displays for visualization of tactile pressures. *Adv Mater Technol*. **2019**;*4*:1900082.
37. Lee T, Kang Y, Kim K, Sim S, Bae K, Kwak Y, Park W, Kim M, Kim J. All paper-based, multilayered, inkjet-printed tactile sensor in wide pressure detection range with high sensitivity. *Adv Mater Technol*. **2022**;*7*:2100428.
38. Pinto JO, Dores AR, Geraldo A, Peixoto B, Barbosa F. Sensory stimulation programs in dementia: a systematic review of methods and effectiveness. *Expert Rev Neurother*. **2020**;*20*:1229.
39. Ladda AM, Pfannmoeller JP, Kalisch T, Roschka S, Platz T, Dinse HR, Lotze M. Effects of combining 2 weeks of passive sensory stimulation with active hand motor training in healthy adults. *PLoS ONE*. **2014**;*9*: e84402.
40. Luo Z, Jose PE, Huntsinger CS, Pigott TD. Fine motor skills and mathematics achievement in East Asian American and European American kindergartners and first graders. *Br J Dev Psychol*. **2007**;*25*:595.
41. Brewer H, Renck Jalongo M, Rule AC, Smith LL. Fine motor skills, executive function, and academic achievement. Cham: Springer; 2018.
42. Suggate S, Pufke E, Stoeger H. Do fine motor skills contribute to early reading development? *J Res Read*. **2018**;*41*:1.
43. Huffman JM, Fortenberry C. Developing fine motor skills. *Young Child*. **2011**;*66*:100.
44. Ahn SN. Combined effects of virtual reality and computer game-based cognitive therapy on the development of visual-motor integration in children with intellectual disabilities: a pilot study. *Occup Ther Int*. **2021**;*2021*:6696779.
45. Lin HC, Chiu YH, Chen YJ, Wuang YP, Chen CP, Wang CC, Huang CL, Wu TM, Ho WH. Continued use of an interactive computer game-based visual perception learning

system in children with developmental delay. *Int J Med Inform*. **2017**;*107*:76.
46. Strom BS, Ytrehus S, Grov EK. Sensory stimulation for persons with dementia: a review of the literature. *J Clin Nurs*. **1805**;*2016*:25.
47. Oliveira J, Gamito P, Souto T, Conde R, Ferreira M, Corotnean T, Fernandes A, Silva H, Neto T. Virtual reality-based cognitive stimulation on people with mild to moderate dementia due to Alzheimer's disease: a pilot randomized controlled trial. *Int J Environ Res Public Health*. **2021**;*18*:5290.
48. Hirt J, Beer T. Use and impact of virtual reality simulation in dementia care education: a scoping review. *Nurse Educ Today*. **2020**;*84*: 104207.
49. Wang L-L, Lee I-J, editors. A preliminary study on application of tangible user interface and augmented reality technology with table game and hand-eye coordination operation tasks in the fields of memory and visuospatial perception for the elderly. In: International conference on human-computer interaction. Springer; **2022**.
50. Jirayucharoensak S, Israsena P, Pan-Ngum S, Hemrungrojn S, Maes M. A game-based neurofeedback training system to enhance cognitive performance in healthy elderly subjects and in patients with amnestic mild cognitive impairment. *Clin Interv Aging*. **2019**;*14*:347.
51. Zhunio CS, Orellana PC, Patiño AV, editors. A memory game for elderly people: development and evaluation. In: 2020 Seventh international conference on eDemocracy & eGovernment (ICEDEG). IEEE; **2020**.
52. Ramnath U, Rauch L, Lambert EV, Kolbe-Alexander T. Efficacy of interactive video gaming in older adults with memory complaints: a cluster-randomized exercise intervention. *PLoS ONE*. **2021**;*16*: e0252016.
53. Poewe W, Seppi K, Tanner CM, Halliday GM, Brundin P, Volkmann J, Schrag A-E, Lang AE. Parkinson disease. *Nat Rev Dis Prim*. **2017**;*3*:1.
54. Roller WC, Glatt S, Vetere-Overfield B, Hassanein R. Falls and Parkinson's disease. *Clin Neuropharmacol*. **1989**;*12*:98.
55. Chatzaki C, Skaramagkas V, Tachos N, Christodoulakis G, Maniadi E, Kefalopoulou Z, Fotiadis DI, Tsiknakis M. The smart-insole dataset: gait analysis using wearable sensors with a focus on elderly and Parkinson's patients. *Sensors (Basel)*. **2021**;*21*:2821.
56. Yang B, Li Y, Wang F, Auyeung S, Leung M, Mak M, Tao X. Intelligent wearable system with accurate detection of abnormal gait and timely cueing for mobility enhancement of people with Parkinson's disease. *Wearable Technol*. **2022**;*3*: e12.
57. Qiu F, Cole MH, Davids KW, Hennig EM, Silburn PA, Netscher H, Kerr GK. Effects of textured insoles on balance in people with Parkinson's disease. *PLoS ONE*. **2013**;*8*: e83309.
58. Lirani-Silva E, Vitorio R, Barbieri FA, Orcioli-Silva D, Simieli L, Gobbi LTB. Continuous use of textured insole improve plantar sensation and stride length of people with Parkinson's disease: a pilot study. *Gait Posture*. **2017**;*58*:495.